Figure S1: Satellite picture of the Irchel campus and its surroundings. The red cross denotes the location of the measurement site. Map data: ©2018 Google Earth – © 2009 GeoBasis-DE/BKG.

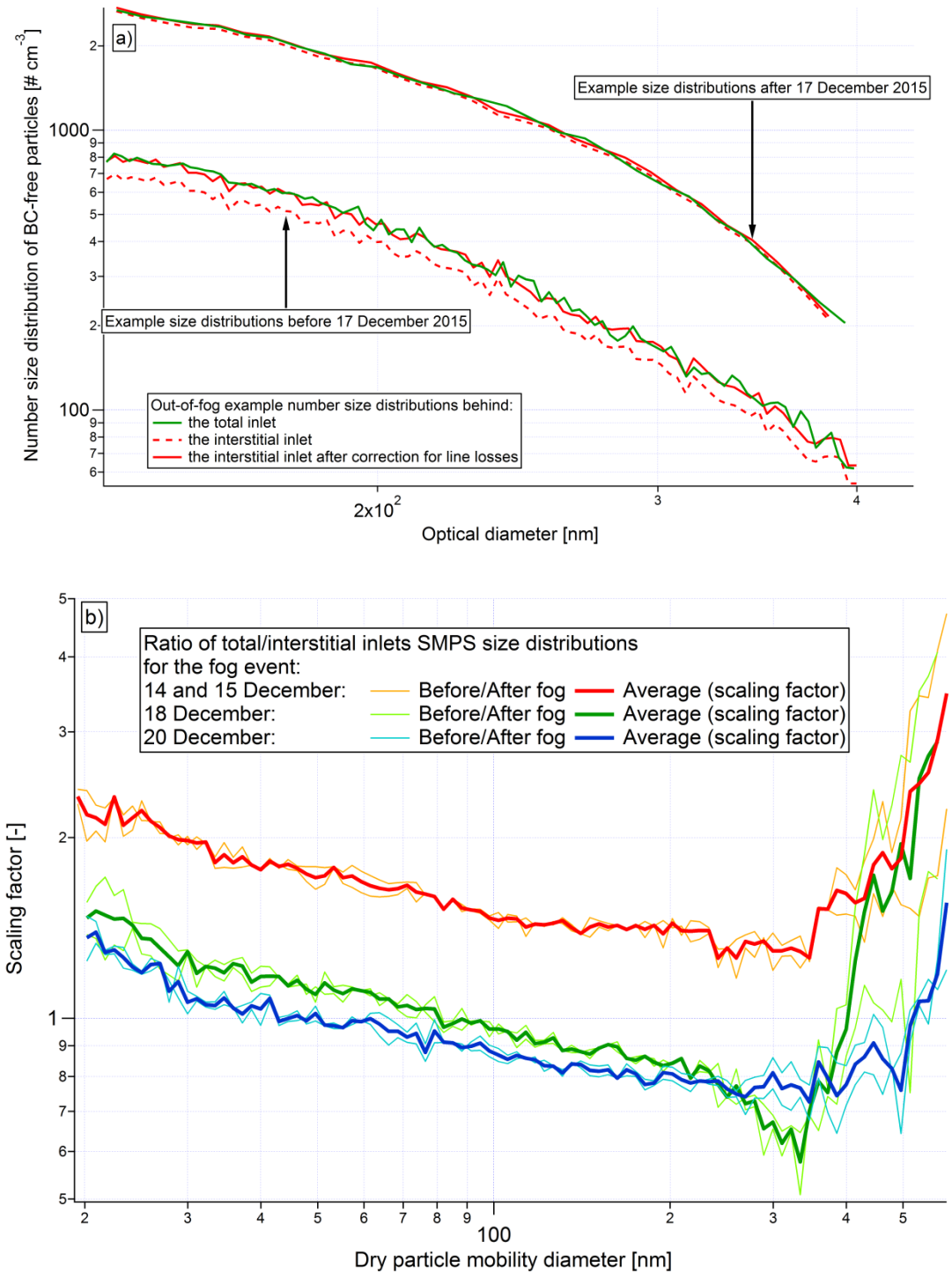

Figure S2: (a) Example SP2-derived particle number size distributions during out-of-cloud conditions showing the corrections made on the interstitial inlet data by the use of scaling factors. A scaling factor of 1.16 was used before 17 December 2015, a factor of 1.03 afterwards (b) Size-dependent scaling factors for correcting SMPS data based on averaged out-of-cloud SMPS measurements before and after each fog event analyzed in this study. The replacement of a conductive tubing on 17 December led to a better agreement between the two instruments. The strong size dependence of the scaling factors can be explained by the fact that they originate from two different instruments, the total-inlet and the interstitial-inlet SMPS. For each fog event, the disagreement between both SMPS was rather stable before and after the event, supporting the assumption that this disagreement did not change during the events.

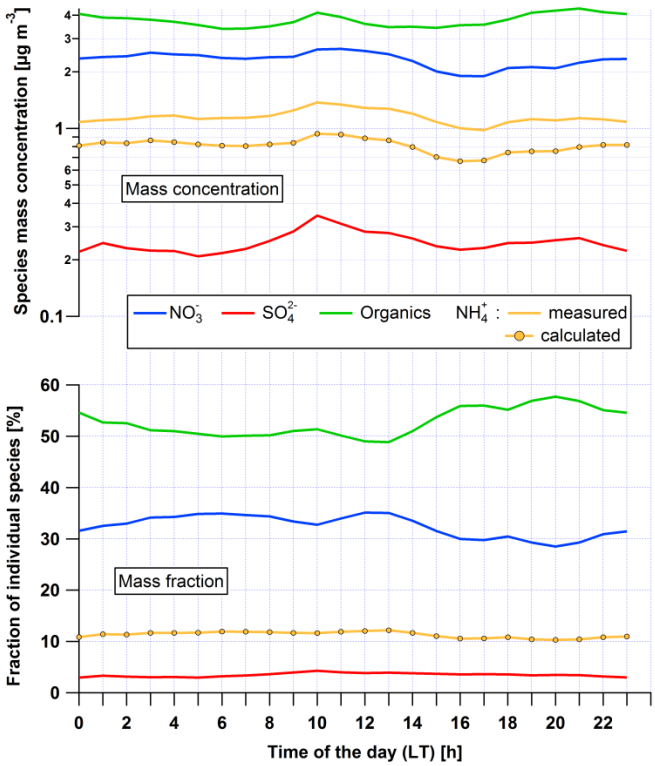

Figure S3:Top: Diurnal variations of mass concentrations measured by the ACSM (top) and corresponding mass fractions (bottom) for the full campaign duration from 6 November 2015 to 31 January 2016. The maximum expected NH_4^+ mass concentration, calculated with assuming that all particulate NO_3^- and SO_4^{2-} was neutralized by NH_4^+ and that no other anions were present in substantial fraction (i.e. n(NH_4^+)=2*n(SO_4^{2-})+n(NO_3^-)), is shown as a dotted line. The measured NH_4^+ mass concentration was higher than this maximum calculated concentration; however, the difference is within measurement uncertainty. Mass fractions of organic matter and salts shown in the bottom panel are based on this calculated maximum NH_4^+ mass concentration.

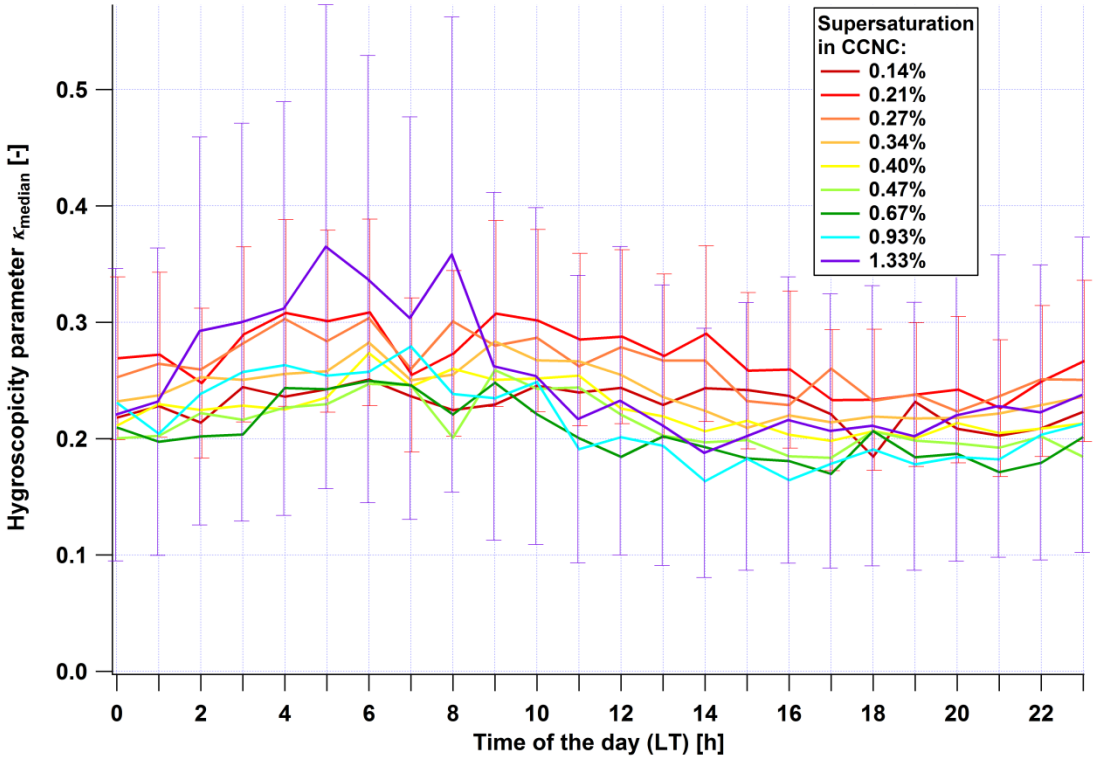

Figure S4: Diurnal patterns of the hygroscopicity parameter κ_{median} extracted from sCCNC measurements and separately averaged by SS for the whole campaign. In accordance with Table 1, the error bars for SS=1.33 % (purple bars) are also representative of SS=0.14 % (dark red line); the error bars for SS=0.21 % (red line) are representative of all other SS.

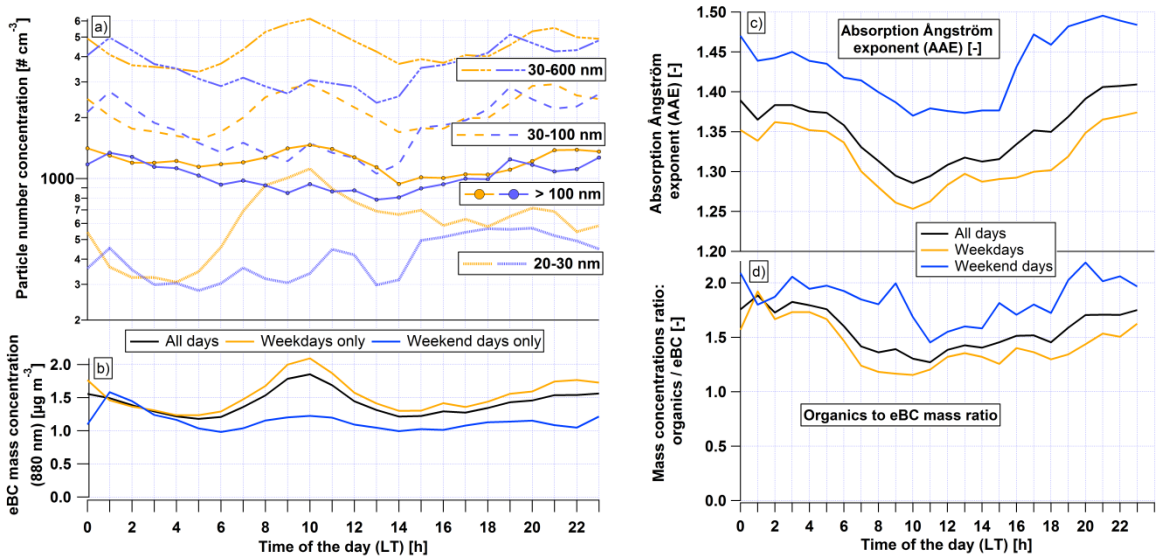

Figure S5: Diurnal patterns for the whole campaign of (a) Number concentration of particles in the nucleation mode (20 to 30 nm), Aitken mode (30 to 100 nm), accumulation mode (>100 nm) and all particles inferred from integrated SMPS data (b) eBC mass concentration inferred from the aethalometer measurement at 880 nm (c) absorption Ångström exponent (AAE) calculated from aethalometer measurements at 470 and 880 nm, and (d) organics (from ACSM) to eBC (from aethalometer) mass concentration ratio. Substantial differences between values of diurnal cycles at 1:00 and at 2:00 can be seen mainly for weekend days, and to a minor extent for weekdays. They are caused by the discontinuities at Friday and Sunday midnight (later corrected to 1:00 from UTC to LT) and limited statistics (particularly for weekend days).

Discussion of Figure S5: To test the hypothesis that the concentration peaks from 8:00 to 10:00 (LT) during weekdays are caused by traffic emissions, we show campaign averaged diurnal patterns of the absorption Ångström exponent (AAE) in Figure S5c. The characteristic values of the AAE for traffic (0.9 to 1) and wood burning (1.47 to 1.80) were previously reported in winter in Zurich (Zotter et al., 2017). In this campaign, the AAE varied between these two ranges, indicating the presence of emissions from both sources. The AAE values are systematically lower during weekdays than weekend days, when almost no heavy duty vehicles, much less light duty vehicles and also less passenger cars are on the road. The minimum AAE value is reached at 10:00 LT during weekdays, in agreement with the concentration peaks seen in Figure S5a,b. Consistent results are found for the diurnal cycles of the organics to eBC mass ratio shown in Figure S5d. Although both traffic and wood combustion contribute to BC and organic emissions, wood burning emissions are associated with much higher organics to BC ratios (Laborde et al., 2013). The lowest values of organics to eBC mass ratios (close to 1) were found during the rush hours of weekdays when traffic emissions dominate. During night time, when wood burning emissions contributed to a much larger extent, the organics to eBC mass ratio increased to around 1.5.

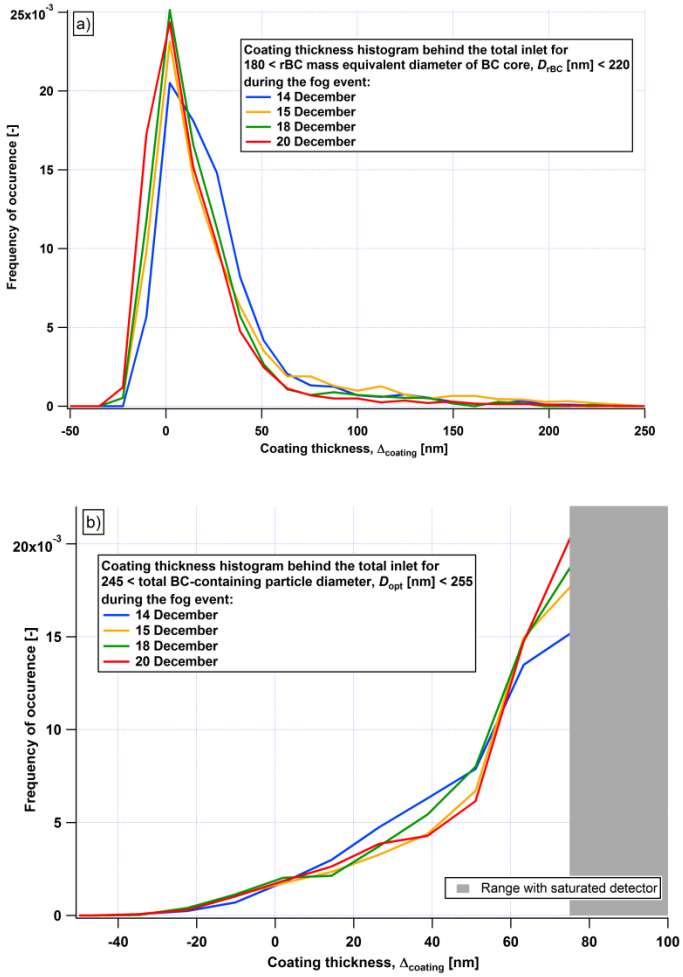

Figure S6: Histograms of BC coating thickness normalized by the area during the analyzed fog events for a fixed BC core diameter range (a) and a fixed total particle diameter range (b).

Figure S6 shows a histogram of the coating thickness of BC cores with a mass equivalent diameter (D_{rBC}) of 200 ± 20 nm during every fog event analyzed. Occurrence of negative coating thickness values, which is derived from independent light scattering and incandescence signals, can have two reasons. First, random noise in the single particle signals causes random noise around the true value in derived single particle coating thickness values. Accordingly, a negative coating thickness will be assigned to half of the uncoated BC cores, however, this is not an issue as the mean coating thickness reported for a particle ensemble will not be biased. Second, systematic calibration biases or inappropriate assumptions in the simplified optical model including refractive indices used to interpret the raw signal can potentially introduce a systematic positive or negative bias in reported coating thickness values. Such potential bias is minimized by comparing the sizing of single BC cores from their incandescence signal (mass-equivalent diameter) and their scattering signal (optical diameter) and ensuring the close agreement between these two quantities. The four histograms in Figure S6a are very similar and show that the dominant fraction of BC-containing particles possess a relatively thin coating, with histograms peaking close to 0 nm (bare BC). This type of analysis, which is relevant for BC core size and thus also BC core mass weighted properties, shows that fresh or recently emitted BC particles dominate over aged BC particles contributed by the background aerosol.

Figure S6b also shows histograms of coating thickness for each fog event analyzed, but in this case including all BC-containing particles with an overall particle optical diameter between 245 nm and 255 nm (as opposed to filtering by similar BC core size as done in in Figure S6a). Again, there is very little variability between the fog events. Here, we find that the dominant fraction of BC cores is thickly coated. The conclusions extracted from these two types of histograms seem to be contradictory but the number size distribution of BC cores (Fig. S7) explains in parts why it is not: BC-containing particles at a fixed overall particle size include either large BC cores without coating or small BC cores with thick coating (or something in between), whereas neither small uncoated BC cores nor large coated BC cores are included. However, the number size distribution peaks way below D_{rBC} = 100 nm and drops steeply between D_{rBC} = 100 nm and 250 nm, therefore, at a given overall particle optical diameter, small aged BC cores are more abundant than large fresh BC cores despite BC mass being dominated by fresh emissions.

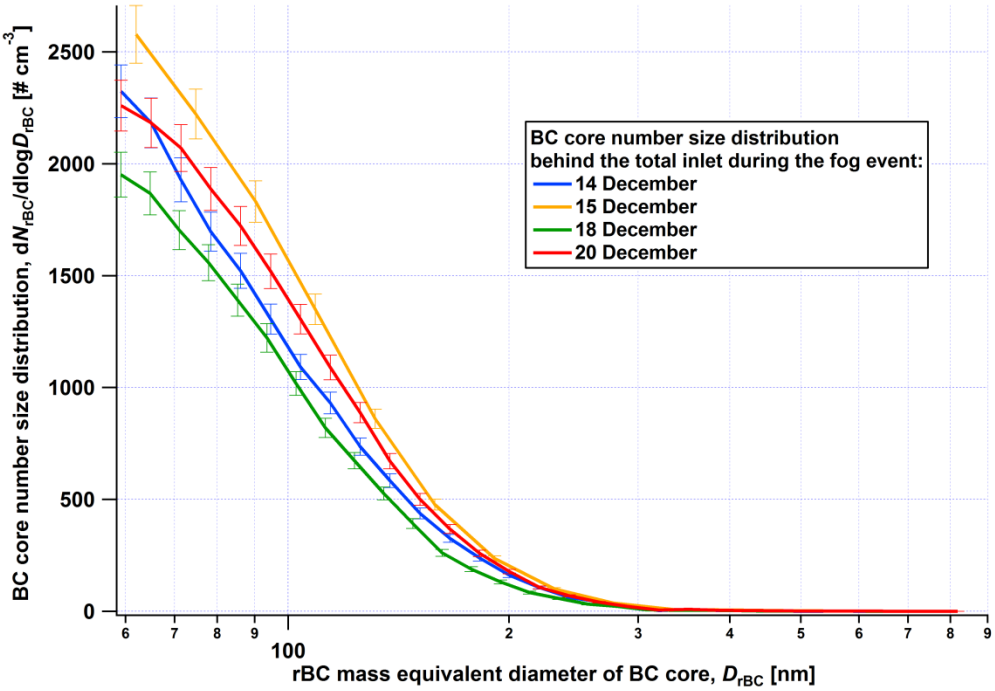

Figure S7: Number size distribution of BC cores during the analyzed fog events (SP2 measurements).

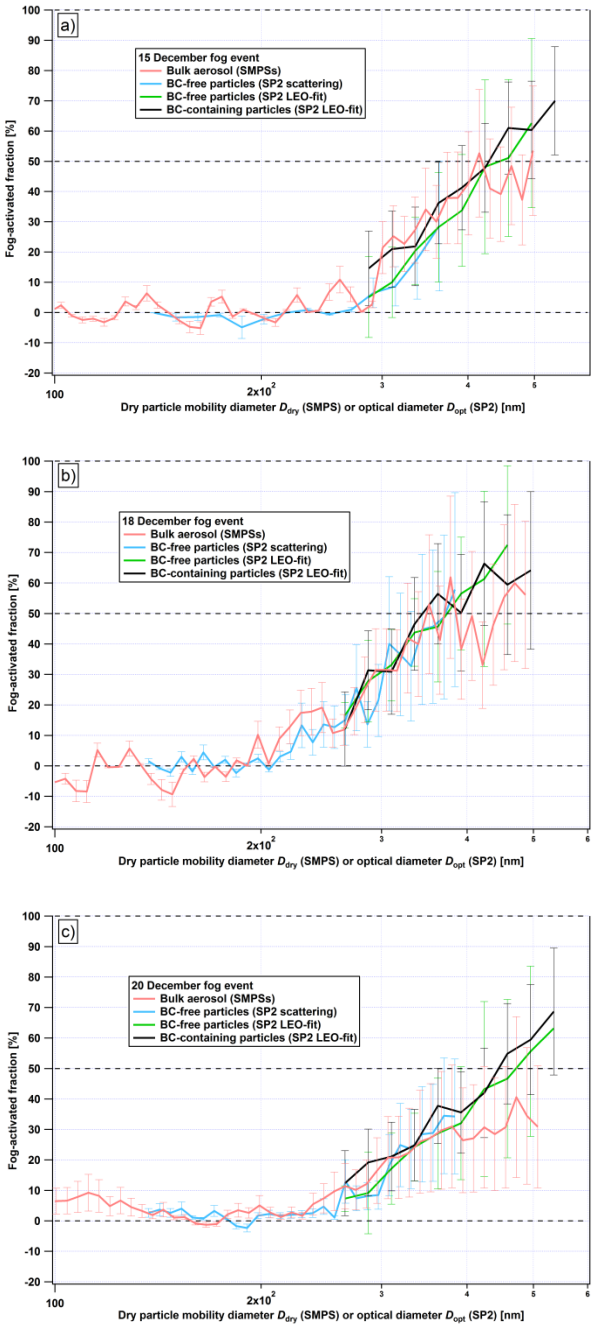

Figure S8: Activated fractions of the bulk aerosol (SMPS, red lines), BC-containing (SP2, black lines) and BC-free particles (SP2 scattering analysis, light blue line and LEO-fit analysis, green lines) during the 15 (a), 18 (b) and 20 (c) December fog events. The 1-σ uncertainties of the BC-containing particle data are Poisson-based with respect to the BC core number size distribution; the other ones are dominated by the level of (dis-)agreement of the interstitial and total measurements, which was determined during out-of-cloud periods and propagated through the calculation of activated fraction.

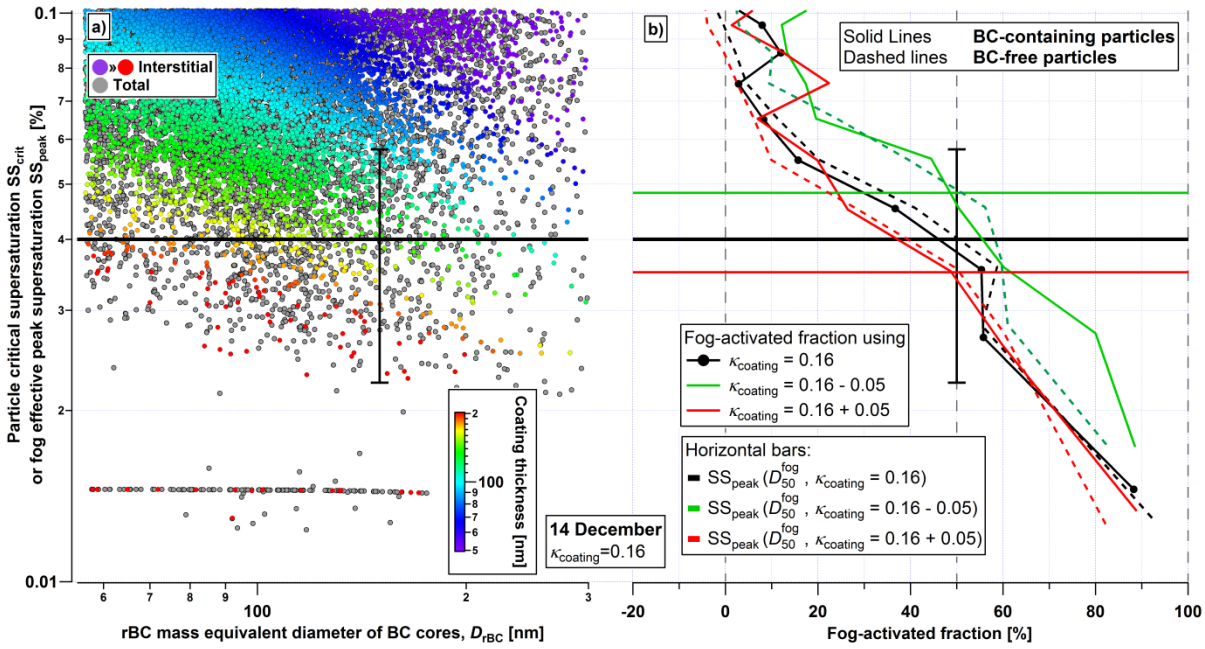

Figure S9: Sensitivity analysis of BC activated fraction in fog to assumed coating hygroscopicity. Same as Figure 9a and b for the 14 December fog event plus additional activation curves derived with $\kappa_{coating}$ disturbed by ±0.05.

Discussion of Figure S9: To infer the critical supersaturation of individual BC-containing particles, the hygroscopicity parameter of the coatings, $\kappa_{coating}$, was assumed to be equal to the median hygroscopicity measured for the total aerosol (κ_{median}; see Sect. 2.3.2). Here, we performed a sensitivity analysis to test the sensitivity of the BC activation closure result to the assumed value of $\kappa_{coating}$: the analysis shown in Figure 9a and 9b and explained in Sect. 3.5 was repeated using $\kappa_{coating}$ disturbed by ±0.05. Figure S9b shows that changing $\kappa_{coating}$ alters the retrieved fog peak supersaturation (solid horizontal lines) as well as the vertical position of the curves indicating the activated fractions. These changes virtually compensate each other such that the observed 50 % activated fraction for BC-containing particles is reached at a supersaturation closely mating the fog peak supersaturation for all three $\kappa_{coating}$ scenarios. This means that successful closure between observed and predicted cloud droplet activation of BC is successfully achieved independent of the exact choice of $\kappa_{coating}$.